



# Patient-specific organotypic blood vessels as an *in vitro* model for anti-angiogenic drug response testing in renal cell carcinoma

José A. Jiménez-Torres<sup>a,b,1</sup>, María Virumbrales-Muñoz<sup>a,b,1</sup>, Kyung E. Sung<sup>c</sup>, Moon Hee Lee<sup>d</sup>, E. Jason Abel<sup>d</sup>, David J. Beebe<sup>a,b,e,\*</sup>

<sup>a</sup> Department of Biomedical Engineering, University of Wisconsin-Madison, 1451 Engineering Dr., Madison, WI 53706, United States of America

<sup>b</sup> University of Wisconsin Carbone Cancer Center, Wisconsin Institutes for Medical Research, 1111 Highland Ave., Madison, WI 53705, United States of America

<sup>c</sup> Division of Cellular and Gene Therapies, Office of Tissues and Advanced Therapies, Center for Biologics Evaluation and Research, The U.S. Food and Drug Administration, Silver Spring, MD 20993, United States of America

<sup>d</sup> Department of Urology, University of Wisconsin, School of Medicine and Public Health, 1111 Highland Ave., Madison, 53705, WI, United States of America

<sup>e</sup> Department of Pathology and Laboratory Medicine, University of Wisconsin, 1111 Highland Ave., Madison, 53705, WI, United States of America

## ARTICLE INFO

### Article history:

Received 30 December 2018

Received in revised form 5 March 2019

Accepted 11 March 2019

Available online 20 March 2019

### Keywords:

Organotypic

Lumen

Model

Anti-angiogenic

Renal

Carcinoma

## ABSTRACT

**Background:** Anti-angiogenic treatment failure is often attributed to drug resistance, unsuccessful drug delivery, and tumor heterogeneity. Recent studies have speculated that anti-angiogenic treatments may fail due to characteristics inherent to tumor-associated blood vessels. Tumor-associated blood vessels are phenotypically different from their normal counterparts, having defective or permeable endothelial monolayers, abnormal sprouts, and abnormal vessel hierarchy. Therefore, to predict the efficacy of anti-angiogenic therapies in an individual patient, *in vitro* models that mirror individual patient's tumor vascular biology and response to anti-angiogenic treatment are needed.

**Methods:** We used a microfluidic *in vitro* organotypic model to create patient-specific biomimetic blood vessels from primary patient-specific tumor endothelial cells (TEnCs) and normal endothelial cells (NEnC). We assessed number of sprouts and vessel organization *via* microscopy imaging and image analysis. We characterized NEnC and TEnC vessel secretions *via* multiplex bead-based ELISA.

**Findings:** Using this model, we found that TEnC vessels exhibited more angiogenic sprouts than NEnC vessels. We also found a more disorganized and gap-filled endothelial monolayer. NEnCs and TEnC vessels exhibited heterogeneous functional drug responses across the five patients screened, as described in the clinic.

**Interpretation:** Our model recapitulated hallmarks of TEnCs and NEnCs found *in vivo* and captured the functional and structural differences between TEnC and NEnC vessels. This model enables a platform for therapeutic drug screening and assessing patient-specific responses with great potential to inform personalized medicine approaches.

**Funding:** NIH grants R01 EB010039, R33 CA225281, R01CA186134 University of Wisconsin Carbone Cancer Center (CA014520), and University of Wisconsin Hematology training grant T32 HL07899.

© 2019 Published by Elsevier B.V. This is an open access article under the CC BY-NC-ND license (<http://creativecommons.org/licenses/by-nc-nd/4.0/>).

## 1. Introduction

Renal cell carcinoma (RCC) is the third most common genitourinary malignancy in the US with ~64,000 new cases and ~14,000 deaths per year [1] and median survival is approximately two years for patients with metastatic disease [2]. A unique feature of RCC is the importance of tumor-associated vasculature [3], which constitutes approximately

25% of the tumor volume, and thereby increases the supply of nutrients and driving tumor growth and metastasis. Consequently, some of the most utilized treatments for RCC are typically anti-angiogenics.

Although the inhibition of angiogenesis has been found to be effective against specific cancers, there are still challenges with determining a treatment plan for each patient. With a substantial number of approved antiangiogenic compounds, no single treatment has proven to be the optimal agent for all patients [4,5]. Conversely, several trials have reported diverse and variable responses among tumors responding to different treatments. That is, while some patients' tumors responded to certain anti-angiogenic treatments resulting in reduced tumor microvessel density, other patients' tumors responded poorly

\* Corresponding author at: Wisconsin Institutes for Medical Research, University of Wisconsin, 1111, Highland Avenue, Madison, WI, United States of America

E-mail address: [djbeebe@wisc.edu](mailto:djbeebe@wisc.edu) (D.J. Beebe).

<sup>1</sup> These authors have contributed to this work equally.

## Research in context

### Evidence before this study

Anti-angiogenic drugs are a major frontline therapy against renal cell carcinoma. However, responses to anti-angiogenic therapies are highly variable, and some patients respond poorly to these drugs. To date, there are few reliable biomarkers to guide clinical decision-making. Hence, there is a clear need for predictive *in vitro* models that can recapitulate drug response for a personalized medicine approach.

### Added value of this study

Here we present an *in vitro* lumen model with primary patient-specific endothelial cells, both from tumor and normal tissue. To our knowledge, this is the first report of a microfluidic model capable of recapitulating hallmarks of the tumor and normal vessels has been reported and validated patient-specific screening of anti-angiogenic drugs.

### Implications of all the available evidence

This model can bring us closer to an *in vitro* personalized medicine approach against renal cell carcinoma and holds great potential for improving clinical decision-making for the treatment of this disease.

or did not respond at all [6]. Anti-angiogenic treatment failure is often attributed to drug resistance, unsuccessful drug delivery, and tumor heterogeneity [7]. Recent studies have speculated that anti-angiogenic treatments may fail due to functional differences between normal and tumor-associated blood vessels, seldom recapitulated *in vitro* [8].

Tumor blood vessels are phenotypically different from their normal counterparts. Tumor-associated endothelial cells (TEnCs), the main component of tumor blood vessels, can produce a defective endothelial monolayer, characterized by higher permeability, abnormal sprouts, abnormal vessel hierarchy, and genetic alterations, as compared to their normal counterparts (NEnCs) [9,10]. Cancer-associated blood vessels have also been reported to be 'leaky', therefore allowing small molecules to move across the vessel walls readily, and thereby increasing responsiveness to exogenous factors such as VEGF and FGF [11]. Most of these findings have focused on identifying the abnormalities of the architecture of tumor blood vessels and their endothelial cells, compared to that of their normal counterparts. However, further elucidation of the functional differences between TEnCs and NEnCs, including differences in angiogenic activity and specific patient response to anti-angiogenic drugs, are critical to understanding why anti-angiogenic drug response is often unpredictable [12]. Therefore, in order to more precisely predict the efficacy of anti-angiogenic therapies in an individual patient, it is critical to have a pre-clinical model that captures these essential differences between TEnCs and NEnCs.

Human Umbilical Cord Vessel Endothelial Cells (HUVEC) have historically been used for angiogenesis research, often with hypoxic or growth factor conditioning to mimic TEnCs [11,13]. However, it is long known that endothelial cells differ in morphology and function (*i.e.*, proliferation, coagulation, chemotaxis) among different organs [14,15], as well as depending on vessel size [16]. HUVEC derive from a large "normal" vessel and are incapable of recapitulating patient-specific tumor heterogeneity [17], therefore they may not be the best cell type to represent tumor-associated capillaries [18]. Alternatively, primary endothelial cells from human tissue explants, xenografts, and *in vivo* models have recently been introduced as essential sources to identify

the genotypic and phenotypic differences between TEnCs and NEnCs [16,19–21]. Human tissue explants may be as close as we can get to the *in vivo* conditions *in vitro*, but these are often difficult to obtain and available in limited quantity.

Additionally, we and others have demonstrated the advantages of microfluidic devices to recreate luminal geometries and structures to study angiogenic migration and sprouting over traditional 2D platforms, such as Petri Dishes, Transwells or Matrigel hydrogels for tube formation assays [22,23]. Mounting evidence highlights differences between cell behavior in 2D and 3D platforms (*e.g.*, the different distribution of mechanical cues affects the migration process, secretion changes), which makes 3D platforms closer to a physiological setting, and therefore recapitulate *in vivo* conditions better [24,25].

Finally, spheroids, a popular 3D *in vitro* model, suffer from well-documented and recurring limitations in reproducibility and imaging [18,26]. Considering these limitations, the use of 3D microfluidic platforms to mimic tubular lumens constitutes a highly customizable alternative to traditional *in vitro* platforms [27], capable of long-term experiments to recapitulate angiogenesis and vascularization processes in a kidney cancer model [17,19,28].

Therefore, we report the generation of an organotypic *in vitro* vessel model with primary endothelial cells that recapitulate the *in vivo* structure of blood vessels and mimic intravenous drug delivery to the endothelial cells. To this end, we used LumeNEXT, a method to create biomimetic blood vessels [22] using primary endothelial cells from RCC patients. The angiogenic capabilities of TEnC and NEnC have been demonstrated in the LumeNEXT model, along with the mimicry of classical hallmarks of *in vivo* TEnC and NEnC vessels; such as an irregular non-confluent endothelial monolayer and higher pro-angiogenic factor secretion. Finally, the functional response of TEnCs and NEnC vessels to two anti-angiogenic agents (*i.e.*, Pazopanib and Sunitinib) was assessed. To our knowledge, this is the first time that the capacity of primary endothelial cells to preserve their *in vivo* features has been leveraged in a microfluidic *in vitro* model to inform personalized medicine. In summary, this *in vitro* biomimetic model demonstrates the functional and structural differences of TEnCs and NEnCs and provides a platform to assess therapeutic drug screening and patient-specific response.

## 2. Materials and methods

### 2.1. Microdevice design and fabrication

Microdevice fabrication is described in more detail in [22]. Briefly, the microfluidic master was fabricated using SU-8 based lithography. Next, the two-layer PDMS microdevices were fabricated using the SU-8 template. The devices were treated with oxygen plasma and bonded to a 60 mm glass bottom Petri dish (MatTek, P50GC-1.5-14-F) and finally sterilized by UV exposure for 15 min before cell culture. The final microdevice comprised a central microchamber to inject a 3D hydrogel and a 340  $\mu\text{m}$ -diameter PDMS rod.

### 2.2. Microdevice setup for lumen seeding

LumeNEXT microdevices [22] (fabrication details in SI) were treated 10 min with 1% poly(ethyleneimine) (Sigma-Aldrich, 03880) in water and with 0-1% glutaraldehyde (Sigma-Aldrich, G6257) in water for 30 min to enhance hydrogel attachment to the PDMS. Devices were washed at least three times with water and thoroughly dried before hydrogel injection. Briefly, Type I rat tail collagen hydrogels were prepared at 6 mg/ml in ice to prevent premature gelation. Using a chilled tip, a mixture of 80  $\mu\text{l}$  of collagen type I (10 mg/ml, BD Biosciences, 354,249); 3.5  $\mu\text{l}$  NaOH 0.5 M (Fisher Scientific, S318); 10  $\mu\text{l}$  PBS 10 $\times$  (Fisher Scientific, BP3991) and 34  $\mu\text{l}$  of PBS was prepared and incubated on ice for 20 min. The pH was then checked with colorimetric strips (Capitol Scientific, PH1170-7). Provided the pH of the mixture be approximately 7-4, the mixture was injected into the LumeNext device,

and polymerized for 5–10 min at room temperature, followed by 20 min at 37 °C. Afterward, the PDMS rods were pulled out of the polymerized collagen gel from the output port resulting in a lumen structure in the collagen gel.

### 2.3. Cell culture and isolation

Primary endothelial cells were grown in Minimum Essential Medium (MEM) with L-Glutamine, supplemented with 10% of FBS (Corning, 45000-734), 1% of Penicillin/Streptomycin (Gibco, 15140-122), 1% of MEM vitamin mixture 100× (Lonza, 13-607C), 0.5% of ITS (Roche, 11074547001) Sodium Pyruvate 1 mM (Lonza, 13-115E), 100 µM of MEM NEEA (ThermoFisher, 11140-050), 0.4 µg/ml of Hydrocortisone (VWR, 101095-150), 5 ng/ml hEGF (Thermo-Fisher Scientific, PHG0311).

The research protocol to obtain tumor and normal adjacent tissue following surgery at the University of Wisconsin Hospital (Madison, WI) was approved by the Institutional Review Board (2011-0719). Informed consent was obtained prior to surgery from patients to use residual tissue. RCC diagnosis was confirmed by a pathologist for all patients. Collected tumor or normal tissue samples (*ca.* 3 cm<sup>3</sup>) were finely minced with sterile scalpel blades and digested in a mixture of MEM (Corning, 10-010-CV), 5 mg/ml of collagenase (Thermo-Fisher 17100017), 5 mg/ml of hyaluronidase (Sigma, H3506), 1 mg/ml of DNase I (Roche, 04716728001), and 1% Penicillin-streptomycin for 4 h at 5% CO<sub>2</sub> and 37 °C. The dissociated tissue samples were filtered through a 70 µm cap filter (Sigma, CLS431751) and cells were collected by centrifugation. Cells were washed three times with growth media. Endothelial cells were isolated using anti-CD31-conjugated magnetic microbeads (Miltenyi Biotec, 130-091-935) and separation columns (Miltenyi Biotec, 130-042-401) according to the manufacturer's instructions. CD31<sup>+</sup> cells were cultured in tissue culture treated 75 cm<sup>2</sup> flasks (Corning, CLS430641U) at a density of 30–60 · 10<sup>3</sup> cells/cm<sup>2</sup> (depending on digestion yield) in growth media at 5% CO<sub>2</sub> and 37 °C for further experiments. Following cell attachment, the media was refreshed every 2–3 days. When cells reached a density of approximately 45 · 10<sup>3</sup> cells/cm<sup>2</sup>, they were washed with PBS (Fisher BioReagents, BP3991, diluted 1:10 with distilled water) trypsinized with 1 ml of 0.025% trypsin-EDTA (Gibco, R001100) for 5 min. Trypsin was neutralized with 5 ml of growth media and the cell suspension was centrifuged at 0.3g for 5 min. Finally, neutralized trypsin was aspirated, and cells were resuspended at the desired concentration.

### 2.4. Verification of endothelial phenotype via qPCR

RNAs were extracted from cells seeded in a confluent 60-mm culture dish. RNA was extracted by using Nucleospin RNA kit (Macherey-Nagel, PA). The lysis step was performed to harvested cells according to the manufacturer's instructions, and the resulting suspension was stored at –80 °C for later RNA extraction. Once extracted as directed, RNA concentration was quantified using Nanodrop. 1 µg of RNA was used for the retrotranscription, which was performed using GoScript™ Reverse Transcriptase (Promega, A5001), according to the manufacturer's instructions.

Custom qPCR primers (Biorad) were used for the genes presented in Supplementary Table 1, where primers are also detailed. Primers were resuspended at a 10× concentration (10 µM) in Nuclease-free water according to the manufacturer's instructions and stored at –20 °C until use. Screened and reference (housekeeping) genes, along with their forward and reverse primers, are detailed in Supplementary Table S1. SsoAdvanced™ Universal SYBR® Green Supermix (Biorad, 1,725,018) was used to perform the qPCR reactions in a Biorad CFX96 Real-Time System according to the manufacturer's instructions to a final qPCR volume of 10 µl. GAPDH was used for normalization of the data. All reactions were performed in triplicate, in three independent experiments and all reaction efficiencies of the primer/probe sets were close to

100%. Target gene expression was normalized using the geometric mean of the mentioned reference gene. Relative gene expression fold changes were determined between the time points of 24 and 72 h using the 2<sup>–ΔΔCt</sup> method. In the case of CD31 and CD146, fold changes were calculated in comparison to epithelial cells from the same patient, whereas TEM1,7,9 were calculated in TEnC and normalized to NEnC.

### 2.5. Cell seeding in lumens

Primary endothelial cells were utilized for experiments at passage two and three, to avoid senescence observed after these passages. Each lumen was loaded with 2 µl of a cell suspension at 50,000 cells/µl. The devices were then incubated for 45 min at 37 °C to allow for cell attachment. After that, lumens were washed three times with 10 µl of growth media to remove excess cells. Media was refreshed every 24 h and conditioned media was collected for multiplex bead-based ELISA quantification.

### 2.6. qPCR characterization of lumens

NEnC and TEnC-lined lumens were cultured for three days. 2 lm per condition were pooled and mRNA was extracted using a Dynabeads™ mRNA DIRECT™ Purification Kit (Thermo Fisher, 61,011) according to manufacturer's instructions. mRNA was reverse transcribed to cDNA using the RT2 First strand kit (Qiagen, 330,401) and cDNA was analyzed by qPCR using a Qiagen RT2 profiler panel (Qiagen, PAHS-024ZA) in a Roche 96-384 thermal cycler. Data was analyzed using the Qiagen online software (<http://pcrdataanalysis.sabiosciences.com/pcr/arrayanalysis.php>) using the 5 reference (housekeeping) genes provided for normalization.

### 2.7. Analysis of secreted factors

Multiplexed protein secretion analysis was performed on both normal and tumor-associated endothelial cells using the Bead-Based ELISA system MAGPIX (Luminex Corp.) with the MilliPlex angiogenesis panel (Millipore, HAGP1MAG-12K) as described elsewhere [29]. Briefly, conditioned media was retrieved from lumens daily, along with maintenance media from empty lumen devices as an internal control. Sample preparation and detection was performed according to the manufacturer's instructions.

To compare the secretion profile of lumens with other cell culture setups, we quantified pro-angiogenic secreted factors in four different platforms for P22 using NEnC and TEnC: lumen, 2D on a petri dish, 2D on top of a collagen hydrogel (6 mg/ml) and embedded in 3D in a collagen hydrogel (6 mg/ml). The procedure for this assay is described in detail in our previous work [25]. In particular, the media/cell ratio was kept constant to account for scale differences in the cell culture setups.

Data were collected with xPonent software (Luminex), and soluble factor concentrations in media were calculated using mean fluorescence intensities.

### 2.8. Monocyte isolation and seeding for immunofluorescence

Glass-bottom 24 well plates (Mattek, P24G-1.0-13-F) destined to seed monocytes were coated with Poly-L-Lysine (PLL, Millipore-Sigma, P7280) under sterile conditions and according to manufacturer's instructions. Briefly, 150 µl of a 100 µg/ml PLL solution was added on top of each well using endotoxin-free pipette tips and incubated for 30 min at room temperature. Next, PLL was aspirated and washed three times with cell culture grade water (Hyclone, SH3052901). PLL-coated surfaces were left to dry at room temperature for 1 h in sterile conditions.

Control monocytes were purified from whole blood using the Miltenyi Biotec MACSxpress Neutrophil Isolation Kit according to the manufacturer's instructions (Miltenyi Biotec, #130-104-434) and

residual red blood cells were lysed using MACSxpress Erythrocyte Depletion Kit (Miltenyi Biotec, #130-098-196). All donors were healthy and exempt of informed consent according to the institutional review board (IRB 2016-0934). Monocytes were resuspended in attachment media (Promocell, C-28051) and seeded at a density of  $7.5 \cdot 10^4$  cell/cm<sup>2</sup> on the PLL-coated glass-bottom wells. After 45 min, monocytes had attached and media was changed to RPMI (ThermoFisher, 11875-093) with 10% FBS and 1% penicillin/streptomycin.

### 2.9. Immunofluorescence staining in 2D

Primary cells grown on a glass-bottom well plate were fixed after two days of culture by incubating with 4% paraformaldehyde (EMScience, 15,700) in PBS for 12 min. Unless specified otherwise, all the steps were performed at room temperature. Cells were washed three times with 0.1% Tween in PBS for 5 min between every step. Cells were permeabilized with 0.2% Triton® X-100 (MP Biomedicals, 807,426) for 20 min and blocked with 3% Bovine Serum Albumin (BSA) (Sigma-Aldrich, A9056) in PBS for 1 h at 4 °C. Cells were incubated with anti-human CD31 (Abcam, ab9498), anti-human CD68 (Abcam, ab213363),

Cells were then stained with 4 µg/ml AlexaFluor 488 goat anti-mouse (Thermo-Fisher, A-11029), 4 µg/ml AlexaFluor 647 goat anti-rabbit (Thermo-Fisher, A-32733), 1:50 Texas Red®-X Phalloidin (5 units) (Life Technologies, T7471) or PE-conjugated Anti-EpCAM [VU-1D9] (Abcam, ab112068) and 50 µg/ml DAPI (Life Technologies, D1306) in 3% BSA overnight at 4 °C.

### 2.10. Immunofluorescence staining in lumens

Cell-lined lumens were fixed after four days of culture by perfusing 4% paraformaldehyde in PBS through the lumen and incubating for 30 min. Lumens were washed three times with 0.1% Tween in PBS for 30 min between every step. Cells were then permeabilized with 0.2% Triton® X-100 for 30 min and blocked with 3% BSA in PBS overnight at 4 °C. Cells were incubated with human anti-VEcadherin (R&D, MAB9381) at 0.5 µg/ml overnight at 4 °C. Cells were then stained with 1:50 Texas Red®-X Phalloidin (5 units), 4 µg/ml AlexaFluor 488 goat anti-mouse and 50 µg/ml DAPI in 3% BSA overnight at 4 °C. Finally, the lumens were washed to remove excess staining and minimize background.

### 2.11. Drug testing in the lumen models

The biomimetic blood vessels were treated with three different concentrations (10 nM, 500 nM, 1 µM) of the anti-angiogenic drugs Pazopanib (Votrient®, Novartis) and Sunitinib (Sutent®, Pfizer). Both drugs were diluted in Dimethyl Sulfoxide (DMSO, D4540, Sigma-Aldrich, St. Louis, MO) to a stock concentration of 10 mM and stored at –80 °C. Drug stocks were diluted in relevant media to the concentrations mentioned above. 10 µl of each drug solution was supplemented to lumens every 24 h. Control vessels were treated with DMSO vehicle (0.1%). Imaging and image analysis are detailed in SI.

### 2.12. Imaging

Brightfield images were acquired on an inverted microscope (IX81, Olympus) using Slidebook 5.0 imaging system (Intelligent Imaging Innovations (3i), Inc.). F-actin and collagen fibers were imaged by using multiphoton laser scanning microscopy (with a second harmonic filter for collagen) and Second Harmonic Generation (SHG) imaging on an optical workstation constructed around a Nikon Eclipse TE300. A MaiTai Deepsee Ti: sapphire laser (Spectra-Physics) excitation source tuned to 890 nm was utilized to generate both multiphoton excitation and SHG. The beam was focused onto the sample with a Nikon 20× Super Fluor

air-immersion lens (numerical aperture (NA) = 1.2). All SHG imaging was detected from the back-scattered SHG signal with a H7422 GaAsP photomultiplier detector (Hamamatsu, Bridgewater, NJ), and the presence of collagen was confirmed by filtering the emission signal with a 445 nm (narrow-band pass) filter (TFI Technologies) to isolate the SHG signal. WiscScan (Laboratory for Optical and Computational Instrumentation, University of Wisconsin-Madison, WI) was used for data acquisition.

### 2.13. Image analysis

For image analysis, regions of interest of the same size were analyzed from each image. Image analysis of lumen confluency was performed using Fiji [30]. For the calculation of the anisotropy index, the macro Fibriltool [31] was employed, and an anisotropy index ranging from 0 (purely isotropic, i.e., random organization) to 1 (perfect fiber orientation, i.e., purely anisotropic) was extracted.

Curvealign 4.0 (Laboratory for Optical and Computational Instrumentation, University of Wisconsin-Madison, WI) was utilized to calculate the orientation of individual fibers [32].

### 2.14. Statistical analysis

All the experiments were repeated at least three times as independent biological repeats. All results are presented as the mean ± standard error of the mean. Data were analyzed using GraphPad Prism v7. Statistical significance was set at  $p < 0.05$ . Normal distribution was assessed by the Shapiro-Wilk test. One-to-one comparisons were performed with a Student's *t*-test with Welch's correction, after passing the Shapiro-Wilk normality test. Histograms depicting distributions of actin fiber orientation were compared *via* the Kolmogorov-Smirnov test, additionally to a Student's *t*-test with Welch's correction to compare the means of the distributions. Multiple comparisons by ANOVA were corrected using the Holm–Sidak test. Where the assumptions of one-way ANOVA were violated, the non-parametric Kruskal–Wallis test was performed followed by Dunn's multiple comparison tests.

## 3. Results

### 3.1. Development of a patient-specific microfluidic kidney endothelial lumen model

We report an organotypic patient-specific blood vessel model, employing both normal (NEnC) and tumor-associated patient-derived endothelial cells (TEnC) for anti-angiogenic drug testing of tyrosine kinase inhibitors in a 3D microenvironment. To this end, primary cells were isolated from normal and tumor tissue of renal cell carcinoma patients (Fig. 1a–b, histologic subtype and clinical information in Supplementary Table S1). After tissue digestion and mechanical dissociation, endothelial cells from both normal and tumor tissue suspensions were isolated using anti-CD31-conjugated magnetic microbead separation columns (Fig. 1c). CD31<sup>+</sup> cells captured in the column were recovered and cultured *in vitro* until confluent. Although modification of cell phenotype could occur as a consequence of 2D cell culture, this step was necessary to isolate enough cells for the downstream experiments. To corroborate the endothelial lineage of the isolated cells, RT-qPCR was performed on the cultured cells' mRNA to evaluate the expression of endothelial cell markers (CD31 and CD146) and Tumor-associated Endothelial cell Markers (TEM1 and 7) (Fig. S1). CD31<sup>+</sup> cells isolated from normal tissue expressed a lower amount of TEM markers and were considered NEnCs. Conversely, CD31<sup>+</sup> cells isolated from tumor tissue expressed higher TEM markers and were considered TEnCs. Although the specific TEM marker profile is specific to each patient, their expression was in all cases much lower in NEnC than in TEnC within the same patient.

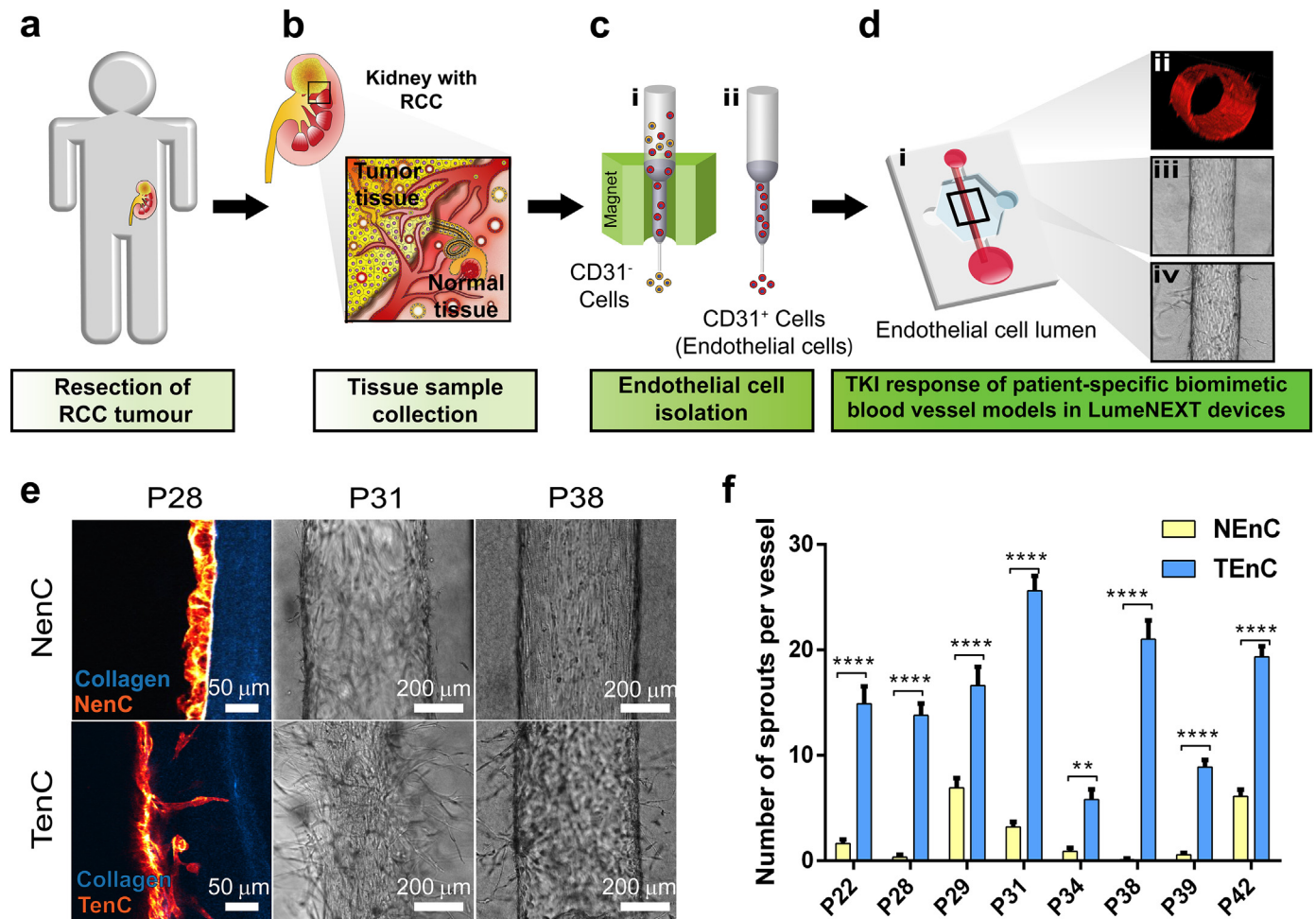


**Fig. 1.** Comparison of angiogenic capabilities of primary renal NEnC and TEEnC. Scheme illustrating the flow of the experimental design. **a)** Clear cell renal cell carcinoma is confirmed in the patient via biopsy, and affected kidney is surgically removed via nephrectomy. **b)** Samples of tumor and adjacent normal tissue are collected from the removed kidney immediately after surgery. **c)** Collected tissue samples are digested and endothelial cells are selected via magnetic bead separation using the surface marker CD31. **d)** Cross-section of the microfluidic luminal structures created in Collagen Type I gels and lined with patient-derived endothelial cells to create biomimetic blood vessels (i). Cross-sectional view of NEnC biomimetic vessel stained with Texas Red phalloidin (ii). Example of vessels before anti-angiogenic treatment (iii) and after treatment (iv) showing the presence of sprouts. **e)** Cross-sectional view of luminal structure for a NEnC and TEEnC vessel from patient 28 (P28) showing phalloidin-stained endothelial cells in red and rat tail collagen type-1 in blue visualized through Second Harmonic Imaging (left). Bright field pictures of NEnC and TEEnC vessels for patient 38 (P38) and 31 (P31) (center and right, respectively). **f)** Number of sprouts generated per area in NEnCs and TEEnCs vessels for different patient samples. (\*\* $p = .049$  for patient 34, and \*\*\*\* $p < .001$  for the rest of the patients, as calculated via two-way ANOVA and Sidak's correction for multiple comparisons). Graphs represent mean  $\pm$  SEM. At least lumens were used, distributed in 3 independent experiments.

We also chose to confirm the lineage of our cells and rule out a significant presence of other contaminating cell types by means of immunofluorescence staining (Supplementary Fig. S2). Particularly, we aimed to exclude the presence of renal epithelial cells (*i.e.* the most abundant cell type in the studied tissue, CD31<sup>-</sup>) using Epcam as marker [33]. We also performed a CD31<sup>+</sup> staining for our NEnC and TEEnC and quantified positive cells to Epcam or CD31 using Hoechst as an internal control.

On the other hand, from all other CD31<sup>+</sup> cells that be present in the tissue and invade our NEnC/TEEnC culture, monocytes or macrophages are the only ones that can adhere and be cultured without specialty media. Other cell types (*e.g.*, platelets) would be washed over the course of 10–14 days that cells take to adhere, expand and colonize the culture flasks. We chose to perform a CD68 (*i.e.*, a canonical marker for neutrophils/macrophages [34]) staining on our NEnC and TEEnC populations to exclude the presence of immune cells. Additionally, we used primary monocytes and the autologous CD31<sup>-</sup> fraction of our primary endothelial cells as positive controls for our anti-CD68 and anti-Epcam antibodies, respectively.

NEnC and TEEnC preparations showed larger cells with different morphology than epithelial cells and primary monocytes. In the latter case,

the difference in size was notorious, indicating that our cell preparations do not contain any immune cell contamination. This is confirmed with the CD68 staining, which was negative in all other cell types, but appears clearly in the positive control (primary monocytes). We also quantified CD31<sup>+</sup> cells in TEEnC and NEnC preparations using Hoechst as an internal control and found that over 98% of the tested cells ( $n =$  at least 500 cells in different fields of view) were CD31<sup>+</sup>.

Finally, we assessed the expression of Epcam in NEnC and TEEnC. Our positive control showed a clear but inhomogeneous stain for this protein, which is common in primary cell samples. Only a few cells in our NEnC preparations were mildly positive for Epcam:  $2.18 \pm 0.346\%$  for TEEnC and  $2.782 \pm 0.527\%$  for NEnC. This indicates that over 97% of the cells in our NEnC and TEEnC preparations are endothelial cells at passage 3. Interestingly, our isotype control was very clean, indicating that our immunofluorescence procedure was robust.

Following positive identification, both normal and tumor endothelial cells were seeded in a LumeNEXT system (Fig. 1d-i) to create patient-specific organotypic blood vessels *in vitro*. A sample image of a 3D-reconstruction of a phalloidin-stained lumen can be found in Fig. 1d-ii, and sample images before and after treatment can be found in Fig. 1d-iii and iv, respectively.

Even though the use of tumor-specific ECM would be ideal, the primary cell isolation process requires the complete digestion of the tissue to release cells, hence destroying the ECM around them. Considering these circumstances, it is unlikely that using tumor-specific ECM is an option in the short term. Further, high heterogeneity in ECM composition has been reported among different patients of renal cell carcinoma. However, these tumors are generally cell-dense and present minimal ECM, which is mostly composed of collagen [35]. Hence, we decided to use rat tail collagen type I [36], which is a popular matrix for the development of organotypic models, easy to use and with lower batch-to-batch variations than commercial protein mixtures (e.g., Matrigel) [37].

Next, the pro-angiogenic potential of primary patient-specific NEnC and TEnC was evaluated in the organotypic lumen model for eight different patients. To this end, both primary cell types were cultured in LumeNEXT to generate lumen structures (representative image of NEnC stained with phalloidin, with orthogonal views is shown in Supplementary Fig. S5 and Video S1). Endothelial sprouts can be seen invading the collagen matrix in Fig. 1e in the case of TEnC lumens, whereas NEnC lumens maintain a straight alignment to the collagen interface. This behavior can be observed in Fig. 1e for patients P31 and P38. The number of sprouts per vessel was quantified for each of the eight assessed patients both in TEnC and in NEnC. Despite high inter-patient heterogeneity, on average TEnC vessels presented 6.38-fold more sprouts than their NEnC counterparts. These results proved statistically significantly different, as assessed with an unpaired *t*-test with Welch's correction ( $***p = 0.0004$ ). When compared within each patient, TEnC lumens presented a significantly higher number of sprouts in all patients ( $****p < 0.0001$ , except for p34, which was  $**p = 0.0049$ ). Increased sprouting and invasion of TEnC as compared to NEnC are consistent with phenotypical differences reported *in vivo* between normal and tumor-associated vessels [10,12].

We also quantified the area occupied by the sprouts on both sides of the lumen and normalized the areas to account for inter-lumen sprout variability (Supplementary Fig. S2B). The results show no significant directionality of sprouts across the different lumens. Finally, we assessed sprout homogeneity along the axis of the lumen. To this end, we defined three Regions of Interest (top, center, bottom, (Supplementary Fig. S2A) in lumens and quantified the area occupied by sprouts (Supplementary Fig. S2C). Areas were within each lumen to account for inter-lumen heterogeneity. Results indicate that differences in area among the three regions are not significant.

### 3.2. Integrity of normal and tumor-associated kidney endothelial cell lumens

An abnormal phenotype has been previously described for tumor-associated blood vessels, including a defective endothelial monolayer, excessive sprouting, and intercellular gaps [38]. These expected features for normal and tumor vessels are illustrated in the schemes shown in Fig. 2a and b, respectively. Therefore, we investigated whether our model recapitulated these distinctive features of normal and tumor vessels, through inspection of F-actin (phalloidin-stained) microscopy images in our vessels. Samples of NEnC and TEnC images can be found in Fig. 2c and d, respectively. At first sight, it can be appreciated how the NEnC vessel presents higher integrity, alignment and a lack of sprouts, unlike the TEnC vessel.

To provide a quantitative analysis of these observations, we first assessed the presence of gaps in the endothelium, also called lumen confluency, through quantification of the surface area of the lumens occupied by phalloidin staining (Fig. 2e). Lumen confluency was  $95.81 \pm 0.5345\%$  for NEnC and  $74.19 \pm 3.717\%$  for TEnC. This difference was found statistically significant ( $**p = 0.010$ ) through Student's *t*-test with Welch correction (Samples passed Shapiro-Wilk normality test).

Next, we determined the anisotropy index with ImageJ Macro Fibriltool [31] (Fig. 2f). This index can be utilized as a measurement of

endothelium organization and homogeneity. NEnC lumens produced an anisotropy index of  $0.2001 \pm 0.03437$ , significantly more anisotropic than TEnC lumens. The latter yielded an index of  $0.09544 \pm 0.0306$  ( $*p = 0.0489$ ), indicating that the F-actin fibers of NEnC are significantly more organized than those of TEnC, which is consistent with Fig. 2c-d.

A lower expression of VE-cadherin is known to occur in TEnC vessels as compared to NEnC [10]. To explore this issue, we performed a VE-cadherin stain, accompanied by Phalloidin and Hoechst staining (Supplementary Fig. S5). We used multiphoton microscopy to reinforce the integrity study of the vessels in our system. Results showed that, whereas the NEnC endothelium was continuous and was covered in all its surface by F-actin or VE-cadherin, large gaps were noticeable in TEnC vessels. Likewise, there was a lower intensity of VE-cadherin in TEnC vessels as compared to NEnC vessels, overall indicating that VE-cadherin has a lower protein expression in TEnC vessels, consistent with previous literature [39].

Finally, we investigated the organization of the F-actin fibers further via CurveAlign [32] analysis, a software capable of determining the angle of orientation of fibrils in a region of interest. For this measurement, we extracted regions of interest parallel to the lumen, and the software calculated the orientation of fibers in relation to the main axis of the lumens. These measurements were extracted both for NEnC and TEnC and are presented in histogram form in Fig. 2g and h, respectively. The distributions look slightly different, with maxima of 39.13% and 26.96% of the fibers oriented in the same direction for NEnC and TEnC, respectively. On average, NEnC actin fibers are oriented at an angle of  $86.60 \pm 1.10^\circ$ , whereas the maximum of the histogram in TEnC actin fibers is oriented at  $79.93 \pm 1.83^\circ$ . This slight difference in orientation was not found to be statistically significant ( $p = 0.6560$ , through Student's *t*-test with Welch correction). However, through Kolmogorov-Smirnov test, which is normally utilized to determine if two distributions are different, they were found to be very significantly different from one another, indicating that TEnC F-actin fibers are far less aligned than those of NEnC, as described in the literature. Overall, the results shown in Fig. 2 indicate that while many of the TEnC actin fibers are oriented parallel to the lumen lining, a significant proportion of them is oriented to other directions, generating a more disorganized and porous structure than in their normal counterparts. These observations are consistent with previously described differences between NEnC and TEnC [10,12].

### 3.3. TEnC lumens express and secrete higher concentrations of pro-angiogenic molecules

After studying morphological differences between NEnC and TEnC lumens we focused on studying differences in lumen protein secretion that might justify the differences in morphology. To this end, we seeded NEnC and TEnC lumens and collected conditioned media on days 3 and 4 after cell seeding (Fig. 3a). We then measured the secretion levels of a panel of growth factors and inflammatory mediators with a multiplex magnetic bead-based immunoassay (*i.e.*, Luminex MAGPIX) (Fig. 3b-c), for two different patients, namely patient 22 and patient 28.

In the case of patient 22, all factors were within a detectable range, and significant differences are observed in the secretion of FGF-2 (8-fold increase), VEGF-A (1.47-fold increase), and Endothelin 1.51-fold decrease) of TEnC as compared to NEnC. These three factors are essential pro-angiogenic mediators.

In contrast, in patient 28, FGF-1 and VEGF-D were not detected, and significant differences are limited to a VEGF-C increase of 2.39-fold in TEnC as compared to NEnC. Both profiles (*i.e.*, increased VEGF and/or increased FGF) are consistent with an increase to the sprouting of TEnC vessels, as compared to NEnC vessels [40,41].

To elaborate on the differences between 2D and 3D cell culture platforms for primary endothelial cells, we performed an additional Luminex MAGPIX assay (Supplementary Fig. S4). In this assay, we

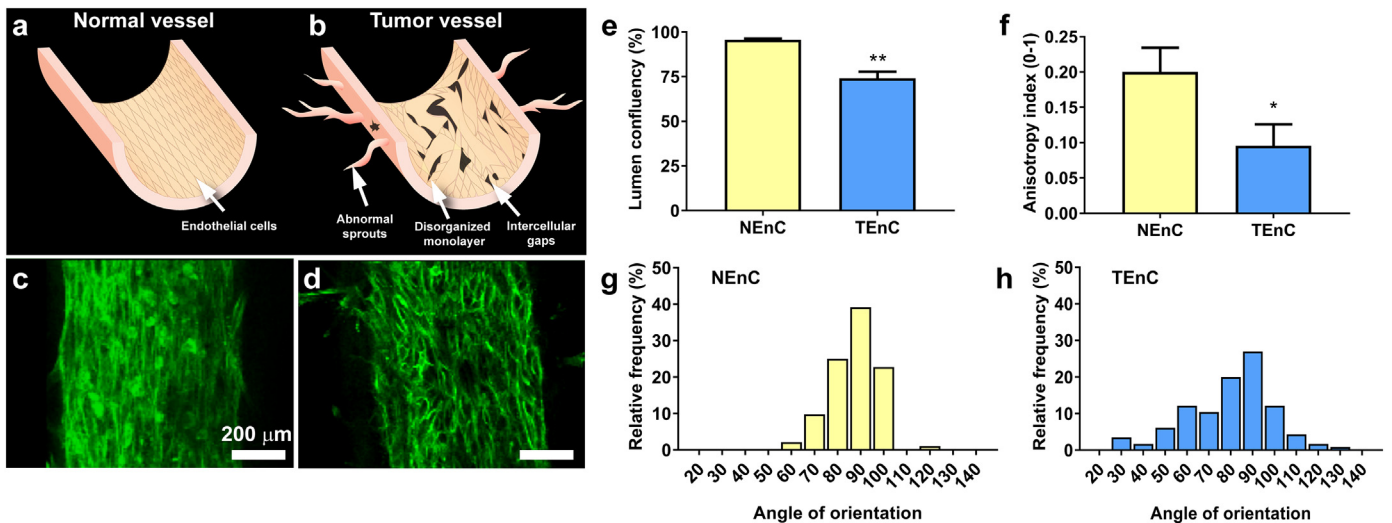


**Fig. 2.** Distinct features of NEnCs and TEnC lumens. A schematic indicating the differences expected between normal and tumor vessels is depicted in **a**) and **b**), respectively. *In vitro* NEnC **c**) and TEnC **d**) phalloidin-stained vessels. **e**) Lumen confluency for NEnC and TEnC lumens (\*\* $p = .001$ ) calculated with F-actin images. **f**) Anisotropy index calculated with Fibriltool ImageJ macro (\* $p = .0489$ ). Histogram of the angle of orientation for F-actin fibers in NEnC lumens **g**) and in TEnC lumens **h**). Calculations were performed using  $90^\circ$  is the axis parallel to the lumen. Comparisons in **e**), **f**) and between **g-h**) were performed with Student's *t*-test with Welch correction after passing the Shapiro-Wilk normality test. Distributions were statistically different \*\* $p = .0091$  via the Kolmogorov-Smirnov test, even though the central tendency was not found to be significantly different between distributions ( $p = .4460$ ). Graphs represent mean  $\pm$  SEM. At least 8 lumens and 2 different patients were used in these experiments.

quantified pro-angiogenic secreted factors in four different platforms for P22 using NEnC and TEnC: lumen, 2D on a petri dish, 2D on top of a collagen hydrogel and embedded in 3D in a collagen hydrogel. We have chosen to present the data for VEGFA due to its importance in the angiogenesis cascade. Results indicate that the only significant difference between NEnC and TEnC is detected in lumens (\*\* $p < .001$ ). Likewise, the production of VEGFA was significantly higher in NEnC and TEnC lumens than any of the other conditions (\*\* $p < .001$ ).

We also performed a comparison of the expression of mRNA transcripts related to the VEGF cascade and cell adhesion and motility, such as *VEGF-A*, *VEGF-C*, *MMP-2* and *14*, *KDR*, *NRP1* and *2* and *CDH5* (Fig. 3d). We tested p51 NEnC and TEnC lumens and calculated the fold change of expression of TEnC over NEnC. Overall, we found a trend of overexpression of pro-angiogenic molecules. Particularly, we found a significant increase in expression of *VEGF-C*, consistent with our MAGPIX findings. We also found a significant increase in *MMP2* and *14*, consistent with the increased sprouting observed in TEnC lumens as compared with NEnC lumens. Likewise, we observed a significant decrease in the expression of *CDH5* (VE-cadherin). This difference was found to be statistically significant ( $p = .0202$ ) which is consistent with the loss of VE-cadherin expression in angiogenic processes [39].

We also observed a trend of increase in certain pro-angiogenic genes, such as *EGF*, *VEGF-A* and *B*, as well as of angiogenic receptors, such as *KDR*, *NRP1* and *2*. However, these trends were not significant, and further studies would need to be performed on this regard to elucidate the role of these molecules in the angiogenic cascade in our system.

#### 3.4. Evaluation of individual tumor vessel model responses to common anti-angiogenic therapies

Finally, we evaluated our organotypic TEnC lumen model to inform personalized medicine treatment decisions by assessing drug response for two popular anti-angiogenic drugs used for mRCC: Pazopanib and Sunitinib. Sunitinib is a small molecule that inhibits multiple receptor tyrosine kinases, including platelet-derived growth factor receptors (PDGFR $\alpha$  and PDGFR $\beta$ ) and vascular endothelial growth factor receptors (VEGFR1, VEGFR2 and VEGFR3) [42]. On the other hand, Pazopanib is a second-generation multitargeted tyrosine kinase inhibitor that

shares primary targets with Sunitinib [43]. Only clear cell renal cell carcinoma patient samples were used for this study, to allow meaningful comparisons (Supplementary Table S1).

Both drugs were used at  $1 \mu\text{M}$  and compared to vehicle control (DMSO). We selected this concentration because it is in the range of concentrations found in human plasma for Pazopanib and Sunitinib [43,44].

Overall, our results showed a variety of responses for these tests in the organotypic TEnC lumen model (results shown as raw number of sprouts are shown in Supplementary fig. S8). For patient 22, treatment with Pazopanib generated sprouting comparable to that of the vehicle control (Fig. 4a), whereas treatment with Sunitinib inhibited the generation of sprouts after 48 h of treatment (Fig. 4b). These results illustrate the potential of this model to recapitulate distinct patient responses to different anti-angiogenic drugs.

Next, lumens from the NEnCs and TEnCs of five different patients were assayed for their response to Sunitinib and Pazopanib (Fig. 4c and d) and compared to vehicle-treated lumens. Interestingly, only TEnC lumens showed an anti-angiogenic response to either Sunitinib or Pazopanib, indicated by negative values (*i.e.*, more sprouts in the vehicle than in the drug-treated organotypic lumens). The fact that NEnC lumens did not respond to anti-angiogenic treatments is consistent with the smaller sprouting potential (and consequently fewer sprouts generated) of NEnC as compared to TEnC, as we showed in Fig. 2, that could mask anti-angiogenic effects. However, some NEnC vessels showed a higher sprouting rate when treated with a particular anti-angiogenic (Fig. 4c, P22 \*\* $p = 0.0072$ ; P39 \*\* $p = 0.0429$ ; P41 \*\* $p = 0.013$ ), whereas others showed no significant changes (P31 and 38). This behavior further illustrates the capacity of our model to mimic the variety of responses that are observed clinically for anti-angiogenic drugs and is consistent with the generation of resistance to these drugs that have been reported in the literature [45–47].

We also compared drug responses between NEnC and TEnC within the same patient (Supplementary fig. S7). Results show that responses for P22 treated with Sunitinib (\*\* $p < .001$ ), P31 treated with Sunitinib and Pazopanib (both \*\* $p < .001$ ), P38 treated with Sunitinib (\*\* $p < .001$ ), and P41 treated with Sunitinib (\*\* $p = .005$ ) were significantly different. In all cases except for P31, TEnC lumens showed decreased

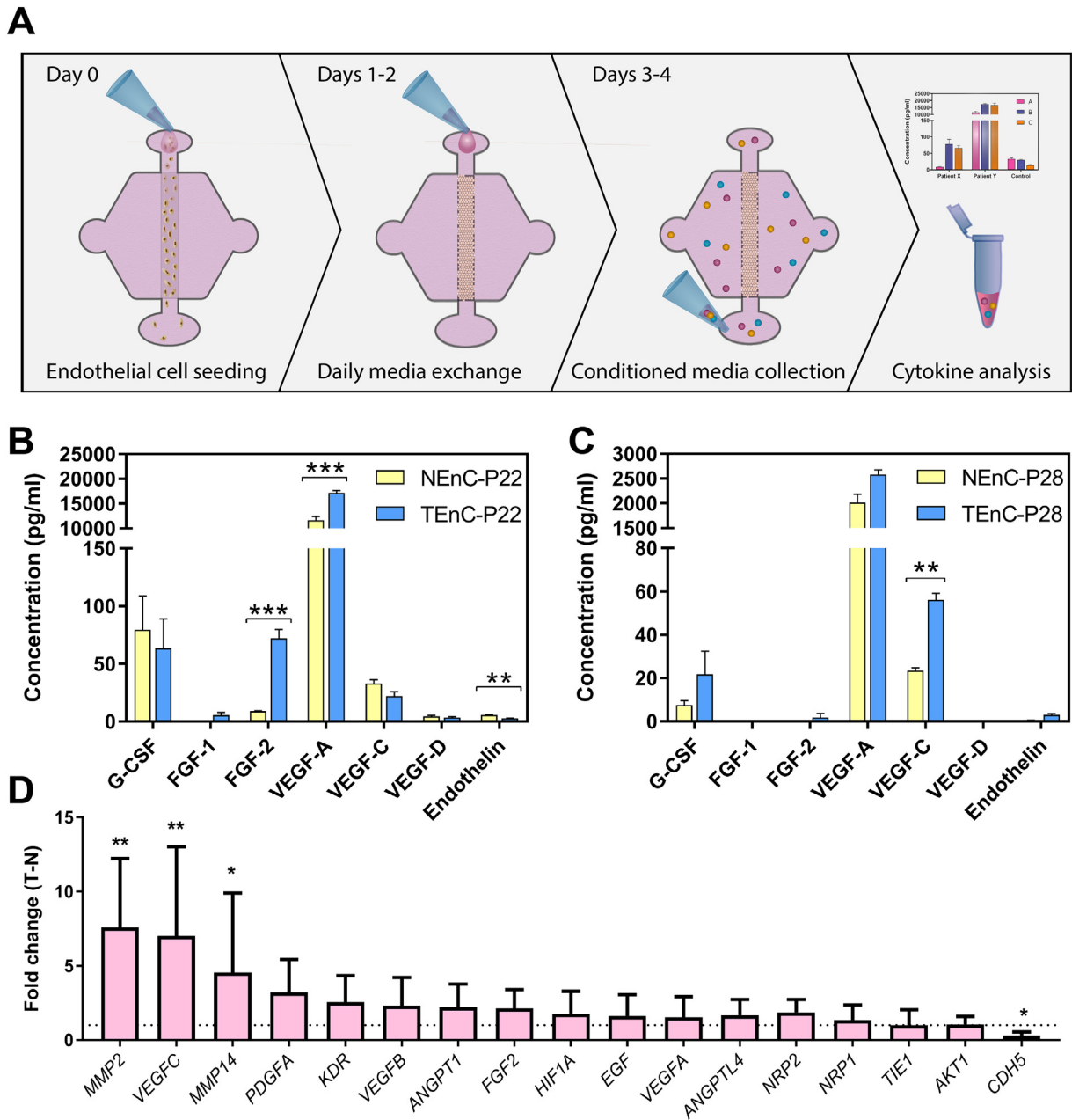


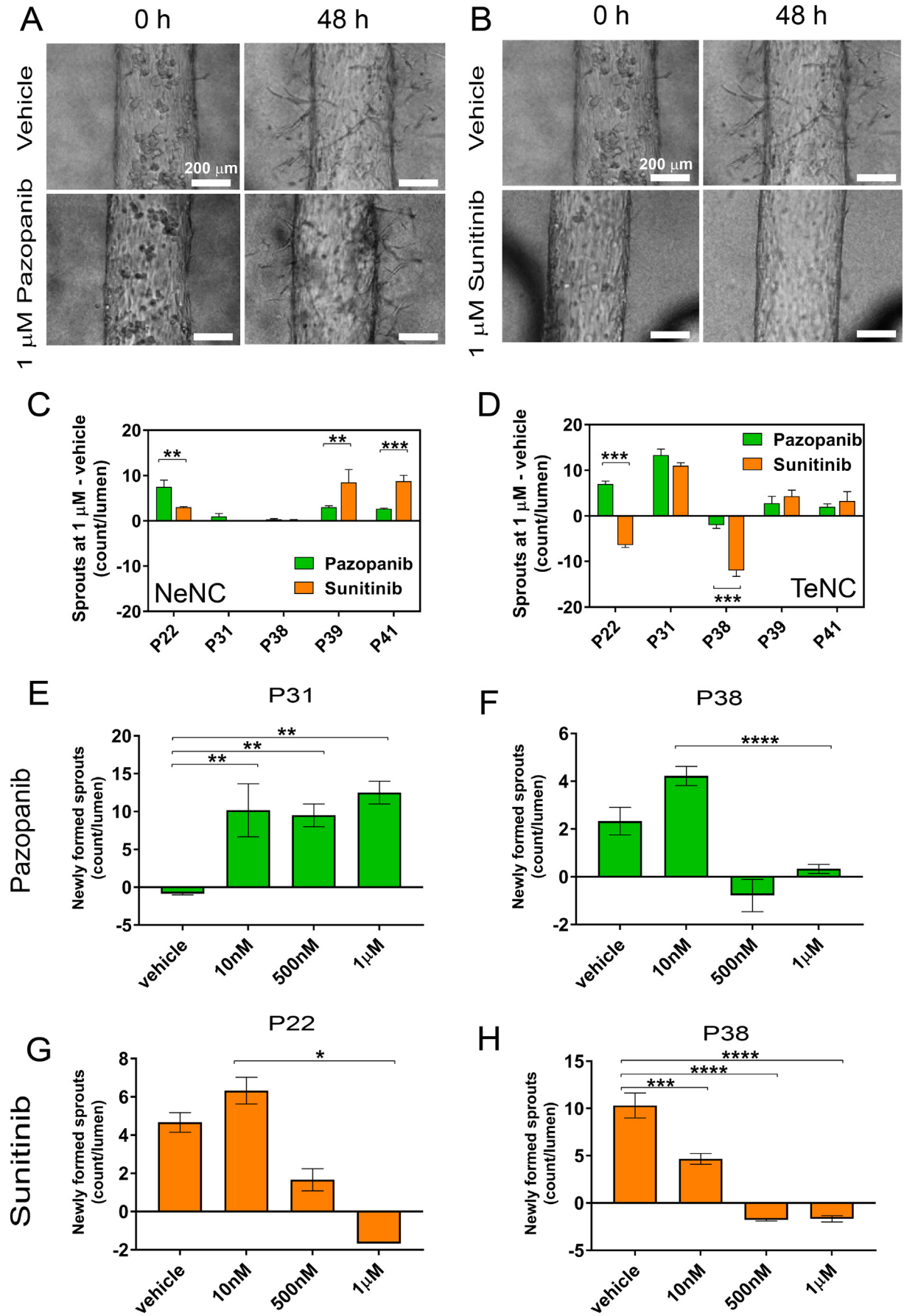
**Fig. 3.** Secretory profile of NEnC and TEnC lumens. **a**) Schematic indicating the seeding procedure and media collection for cytokine analysis. *In vitro* vessel secretion for inflammatory and angiogenic cytokines (G-CSF, FGF-1, FGF-2, VEGF-A, VEGF-C, VEGF-D, and Endothelin) in normal and tumor endothelial cells are depicted in **b**) and **c**) for patient 22 and patient 28 respectively, illustrating inter-patient heterogeneity. Comparisons were performed between NEnC and TEnC via multiple Student's *t*-tests with false discovery rate method of Benjamini, Krieger and Yekutieli. ( $n = 3$ , pooled samples over two days from at least six lumens) **d**) qPCR characterization of differences between NEnC and TEnC lumens. Expression fold changes of angiogenesis-related markers were calculated for primary NEnC and TEnC lumens from patient 51 and results of TEnC lumens were normalized to NEnC lumens. Graphs represent mean  $\pm$  SEM. ( $n = 3$ , pooled samples from at least two lumens.)

sprouting after treatment when compared with DMSO control (smaller values in TEnC than NEnC). However, P31 showed a dramatic increase in sprouting for both Sunitinib and Pazopanib-treated lumens.

Likewise, only some patients-specific TEnC models responded to anti-angiogenic therapies. This fact is consistent with the heterogeneity of responses observed clinically, and the appearance of resistance to anti-angiogenic therapies [10,46]. Additionally, the nature of the responses was heterogeneous as well. Specifically, only TEnC vessel models from patients 22 and 38 showed responses to the anti-angiogenic drugs. The organotypic model for patient 22 showed a decrease in sprouting compared to vehicle control only for Sunitinib ( $***p > 0.0001$ ), whereas model from patient 38 showed a decrease with both drugs, but significantly better for the model treated with

Sunitinib ( $***p > 0.0001$ ). These results highlight the potential of these models to evaluate each patient's response to different anti-angiogenic drugs and inform clinical decision making.

Finally, we explored the capabilities of our model to perform sample dose-response experiments, which could help prevent undesirable side-effects while ensuring drug response in patients. Responses of the lumen models to vehicle control, 10 nM, 500 nM and 1  $\mu$ M of Pazopanib are shown for P31 (Fig. 4e) and P38 (Fig. 4f). For P31 models, we observed a significant increase in sprouting following all doses of Pazopanib ( $**p > 0.095$ ), whereas P38 lumen models responded to doses of 500 nM and 1  $\mu$ M. Similar behavior is observed for P22 lumen models treated with Sunitinib (Fig. 4g,  $*p = 0.0182$ ). However, P38 lumen models responded with a significant decrease of sprouting to



all doses of Sunitinib (Fig. 4h, \*\* $p > 0.014$ , \*\*\* $p > 0.0001$ ). These results provide a proof-of-concept for the evaluation of different doses of the drug of interest, which have been previously shown to play a critical role in the treatment with anti-angiogenic drugs [48].

#### 4. Discussion

Over the last decade, there has been an increase in the number of approved treatment options for metastatic renal cell carcinoma [49], most of which are anti-angiogenic agents. However, recent literature highlights the variability of patient and tumor responses to anti-angiogenic drugs. In other words, while some patients showed an excellent response to a particular anti-angiogenic drug, some others would show a poor response to the same drug [46]. Hence, there is a concomitant need for improved data to aid oncologists in choosing the drug with the highest chance of success for each individual patient. To that end, we present a patient-specific *in vitro* organotypic blood vessel model. To generate this model, we used patient-derived endothelial cells, from both tumor (TEnc) and normal (NEnC) tissue. In our model, TEnc vessels generated more angiogenic sprouts without the addition of exogenous angiogenic growth factors when compared to NEnCs from the same patient tissue.

Furthermore, the NEnC and TEnc biomimetic blood vessels recapitulated hallmarks of normal and tumor vasculature found *in vivo*. Specifically, in TEnc vessels, the cellular organization was more random, and there was an increase in the number of gaps in the endothelium. Furthermore, we showed that the biomimetic blood vessel secretion of key pro-angiogenic factors was different for TEnc and NEnC vessels and that secretion profiles were variable among patients. In all cases, TEnc vessels secreted more pro-angiogenic factors than their normal counterparts, consistently with the more sprout-bound phenotype we showed in this paper. More importantly, this system was tested as a possible clinical assay platform to inform treatment decisions. Our findings show heterogeneity in drug response of endothelial cells between different patients of a similar scope to those observed clinically [50]. Interestingly, TEnc vessels responded more favorably to anti-angiogenic drugs than NEnC vessels: for some patients, anti-angiogenic drugs increased sprouting in NEnC vessels, which similar to observations of resistance to anti-angiogenic therapies often found clinically [47]. Likewise, the response to different anti-angiogenic drugs was also different within the different patient-specific models, and among the different patient-specific models.

A possible explanation to the increased sprouting after anti-angiogenic drug treatment is the presence of multiple and highly redundant mechanisms leading to increased cell motility in the angiogenic cascade. Due to the high redundancy of the cascade, and according to reported resistance mechanisms, responses to anti-angiogenic drugs can be variable [20,21]. This scenario is consistent with our findings and with the highly variable response and a high degree of resistance to anti-angiogenics observed in the clinic [22,23].

Recently, scientific literature has emphasized the value of using functional endpoints to assess anti-cancer drug-responses *in vitro*. This high value is due to the complexity and redundancy of signaling pathways responsible for cancer hallmarks, the significance of which depends on the tumor's underlying molecular features and environment [51,52]. Hence, the use of molecular endpoints to assess drug response of anti-cancer drugs is a non-trivial task. In contrast, the use of functional endpoints that inherently integrate *in vivo* processes should

lead to more predictive endpoints and next-generation personalized medicine approaches. Our work in this paper leverages the use of functional endpoints to provide additional information to a clinically relevant problem that requires more attention from the scientific community. This model opens the door to future prospective studies, in which follow-up data on each patient's drug response can be accessed and compared to *in vitro* responses to functional assays. Ideally, an organotypic model-based functional approach would take advantage of standard-of-care tumor resection to acquire tissue and provide a personalized treatment option when the patient has recovered from surgery and can start a treatment régime. However, a limitation of this approach would be the difficulty in recreating secondary tumor sites, due to the limited size of metastases.

The microenvironment is a very complex niche that harbors many different cell types, which are known to contribute to the angiogenesis process [40]. The incorporation of many cell types complicates assays and increases the complexity of experimental design and experiments themselves. However, there is a need to understand the role that these different microenvironment components play in predicting drug response to anti-angiogenics [53]. To this end, our findings provide a platform to develop further models where a tumor can be placed next to a biomimetic blood vessel to mimic tumor angiogenesis *in vitro*. As well as the interaction among different cell types in the tumor microenvironment, our model holds great potential to study the diffusion and penetration of substances through the capillaries and into the tumor sites. These substances could range from glucose and nutrients to therapeutic molecules or antibodies [54]. Regarding the use of therapeutic antibodies, with immunotherapies on the rise and recently approved for treatment against RCC [55], our model is amenable to study the efficacy of immunotherapies alone or in combination with anti-angiogenic therapies for each patient.

Many authors have reported the profound effect of shear stress induced by fluid flow in endothelial cell morphology and function [56–58]. Endothelial cells have been reported to acquire an elongated and aligned morphology in the presence of flow, as opposed to the polygonal shape they exhibit in 2D static cultures [59]. Likewise, many functional differences (*e.g.*, vascular integrity, proliferation, mechanosensing, and homeostasis) have been reported to vary because of fluid flow, and due to flow persistence and shear stress value [60]. While the application of fluid flow is out of the scope of our paper, we have observed this morphology change in our models, after daily washes and media changes *via* passive pumping mechanisms. Further studies would need to be performed to determine the specific role of fluid flow in patient-derived endothelial cells in anti-angiogenic response in renal cell carcinoma. We anticipate these and further issues will be explored soon.

Overall, with this model we can move steps closer to having a patient-derived *in vitro* model that can complement animal models and provide predictive value to inform clinical decision.

#### Acknowledgments

Special thanks to Dr. Lauren Bischel who supervised the beginnings of this project, Dr. Matthew Conklin for help in operating CurveAlign, and Dr. Sheena Kerr for performing the monocyte isolation and for assistance with immunofluorescence staining. The authors would like to thank the University of Wisconsin Carbone Cancer Center (UWCCC) for the use of its Shared Services to complete this research. NIH grants R01 EB010039, R33 CA225281–01, R01CA186134 University of

**Fig. 4.** Drug response of NEnC and TEnc lumens. Representative bright field images of TEncs vessels for patient 22 treated with vehicle (DMSO) or an antiangiogenic agent. Results are shown for 1  $\mu$ M of Pazopanib **a**) and 1  $\mu$ M of Sunitinib at 0 and 48 h after drug treatment, as number of sprouts present in the treated lumens, minus the sprouts of the vehicle control. Responses of NEnC **c**) and TEnc **d**) lumens, quantified as the number of sprouts per lumen minus the sprouts of the vehicle control are shown for five different patients (22, 31, 38, 39 and 41), both to Sunitinib and Pazopanib. Dose-response curves of TEnc lumens to Pazopanib of lumens from patients 31 and 38 **e-f**) and Sunitinib **g-h**) for patients 22 and 38, illustrating inter-patient heterogeneity. Graphs represent mean  $\pm$  SEM. At least three lumens were used with three independent experiments performed per condition.

Wisconsin Carbone Cancer Center (CA014520), and University of Wisconsin Hematology training grant T32 HL07899

## Declaration of conflict of interests

David J. Beebe holds equity in Bellbrook Labs, LLC, Tasso Inc., Salus Discovery LLC, Lynx Biosciences, Inc., Stacks to the Future, LLC, Turba LLC, and Onexio Biosystems, LLC.

## Author contributions

J.A.J., D.J.B., E.J.A., K.E.S. designed the study. E.J.A. performed the surgeries and collected the samples. J.A.J., K.E.S. and M.H.L performed the experiments. J.A.J., M.V., M.H.L analyzed the data. J.A.J., M.V. and K.E.S interpreted the data. J.A.J., M.V., K.E.S., E.J.A., D.J.B. wrote the manuscript.

## References

- [1] Siegel RL, Miller KD, Jemal A. Cancer statistics, 2017. *CA Cancer J Clin* 2017;67(1):7–30.
- [2] Heng DY, Xie W, Regan MM, Harshman LC, Bjarnason GA, Vaishampayan UN, et al. External validation and comparison with other models of the international metastatic renal-cell carcinoma database consortium prognostic model: a population-based study. *Lancet Oncol* 2013;14(2):141–8.
- [3] Chism DD, Rathmell WK. Kidney cancer: rest ASSURED, much can be learned from adjuvant studies in renal cancer. *Nat Rev Nephrol* 2016;12(6):317–8.
- [4] Cao R, Ji H, Feng N, Zhang Y, Yang X, Andersson P, et al. Collaborative interplay between FGF-2 and VEGF-C promotes lymphangiogenesis and metastasis. *Proc Natl Acad Sci* 2012;109(39):15894–9 [201208324].
- [5] Gotink KJ, Verheul HM. Anti-angiogenic tyrosine kinase inhibitors: what is their mechanism of action? *Angiogenesis* 2010;13(1):1–14.
- [6] Lupo G, Caporarello N, Olivieri M, Cristaldi M, Motta C, Bramanti V, et al. Anti-angiogenic therapy in cancer: downsides and new pivots for precision medicine. *Front Pharmacol* 2017;7:519.
- [7] Vasudev NS, Reynolds AR. Anti-angiogenic therapy for cancer: current progress, unresolved questions and future directions. *Angiogenesis* 2014;17(3):471–94.
- [8] Al-Abd AM, Alamoudi AJ, Abdel-Naim AB, Neamatallah TA, Ashour OM. Anti-angiogenic agents for the treatment of solid tumors: potential pathways, therapy and current strategies—a review. *J Adv Res* 2017;8(6):591–605.
- [9] Lang JM, Harrison MR. Pazopanib for the treatment of patients with advanced renal cell carcinoma. *Clin Med Insights Oncol* 2010;4:95–105 [Epub 2010/10/29].
- [10] Dudley AC. Tumor endothelial cells. *Cold Spring Harb Perspect Med* 2012;2(3):a006536. Epub 2012/03/07.
- [11] Hida K, Maishi N, Torii C, Hida Y. Tumor angiogenesis—characteristics of tumor endothelial cells. *Int J Clin Oncol* 2016;21(2):206–12.
- [12] Hida K, Maishi N, Annan DA, Hida Y. Contribution of tumor endothelial cells in cancer progression. *Int J Mol Sci* 2018;19(5).
- [13] Krock BL, Skuli N, Simon MC. Hypoxia-induced angiogenesis: good and evil. *Genes Cancer* 2011;2(12):1117–33.
- [14] Fajardo LF. Special report the complexity of endothelial cells: a review. *Am J Clin Pathol* 1989;92(2):241–50.
- [15] Lai X, Witzmann FA, Yoder MC. Venous and arterial endothelial proteomics: mining for markers and mechanisms of endothelial diversity AU – Richardson, Matthew R. *Expert Rev Proteomics* 2010;7(6):823–31.
- [16] Bouis D, Hospers GAP, Meijer C, Molema G, Mulder NH. Endothelium in vitro: a review of human vascular endothelial cell lines for blood vessel-related research. *Angiogenesis* 2001;4(2):91–102.
- [17] Staton CA, Reed MW, Brown NJ. A critical analysis of current in vitro and in vivo angiogenesis assays. *Int J Exp Pathol* 2009;90(3):195–221.
- [18] Nowak-Sliwinska P, Alitalo K, Allen E, Anisimov A, Aplin AC, Auerbach R, et al. Consensus guidelines for the use and interpretation of angiogenesis assays. *Angiogenesis* 2018;21(3):425–532.
- [19] Hirakawa S, Hong Y-K, Harvey N, Schacht V, Matsuda K, Libermann T, et al. Identification of vascular lineage-specific genes by transcriptional profiling of isolated blood vascular and lymphatic endothelial cells. *Am J Pathol* 2003;162(2):575–86.
- [20] St Croix B, Rago C, Velculescu V, Traverso G, Romans KE, Montgomery E, et al. Genes expressed in human tumor endothelium. *Science* 2000;289(5482):1197–202 [Epub 2000/08/19].
- [21] Bussolati B, Deambrosio I, Russo S, Deregibus MC, Camussi G. Altered angiogenesis and survival in human tumor-derived endothelial cells. *FASEB J* 2003;17(9):1159–61.
- [22] Jiménez-Torres JA, Peery SL, Sung KE, Beebe DJ. LumeNEXT: a practical method to pattern luminal structures in ECM gels. *Adv Healthc Mater* 2016;5(2):198–204.
- [23] Verbridge SS, Chakrabarti A, DelNero P, Kwee B, Varner JD, Stroock AD, et al. Physicochemical regulation of endothelial sprouting in a 3D microfluidic angiogenesis model. *J Biomed Mater Res A* 2013;101(10):2948–56 [Epub 2013/04/06].
- [24] Baker BM, Chen CS. Deconstructing the third dimension—how 3D culture microenvironments alter cellular cues. *J Cell Sci* 2012;125(13):3015–24.
- [25] Bischel LL, Sung KE, Jiménez-Torres JA, Mader B, Keely PJ, Beebe DJ. The importance of being a lumen. *FASEB J* 2014;28(11):4583–90.
- [26] Ayuso JM, Virumbrales-Munoz M, Lacueva A, Lanuza PM, Checa-Chavarría E, Botella P, et al. Development and characterization of a microfluidic model of the tumour microenvironment. *Sci Rep* 2016;6.
- [27] Bhatia SN, Ingber DE. Microfluidic organs-on-chips. *Nat Biotechnol* 2014;32(8):760–72.
- [28] Miller CP, Tsuchida C, Zheng Y, Himmelfarb J, Akilesh S. A 3D human renal cell carcinoma-on-a-chip for the study of tumor angiogenesis. *Neoplasia* (New York, NY) 2018;20(6):610–20 [Epub 2018/05/11].
- [29] Ingram PN, Hind LE, Jimenez-Torres JA, Huttenlocher A, Beebe DJ. An accessible organotypic microvessel model using iPSC-derived endothelium. *Adv Healthc Mater* 2018;7(2):1700497.
- [30] Schindelin J, Arganda-Carreras I, Frise E, Kaynig V, Longair M, Pietzsch T, et al. Fiji: an open-source platform for biological-image analysis. *Nat Methods* 2012;9(7):676–82 [Epub 2012/06/30].
- [31] Boudaoud A, Burian A, Borowska-Wykret D, Uyttewaal M, Wrzaliak R, Kwiatkowska D, et al. FibrilTool, an ImageJ plug-in to quantify fibrillar structures in raw microscopy images. *Nat Protoc* 2014;9(2):457–63.
- [32] Bredfeldt JS, Liu Y, Pehlke CA, Conklin MW, Szulzewski JM, Inman DR, et al. Computational segmentation of collagen fibers from second-harmonic generation images of breast cancer. *J Biomed Opt* 2014;19(1):16007. Epub 2014/01/11.
- [33] Maetzel D, Denzel S, Mack B, Canis M, Went P, Benk M, et al. Nuclear signalling by tumour-associated antigen EPCAM. *Nat Cell Biol* 2009;11(2):162.
- [34] Holness CL, Simmons DL. Molecular cloning of CD68, a human macrophage marker related to lysosomal glycoproteins. *Blood* 1993;81(6):1607–13.
- [35] Droz D, Patey N, Paraf F, Chretien Y, Gogusev J. Composition of extracellular matrix and distribution of cell adhesion molecules in renal cell tumors. *Lab Invest* 1994;71(5):710–8.
- [36] Antoine EE, Vlachos PP, Rylander MN. Review of collagen I hydrogels for bioengineered tissue microenvironments: characterization of mechanics, structure, and transport. *Tissue Eng Part B Rev* 2014;20(6):683–96.
- [37] Jabaji Z, Brinkley GJ, Khalil HA, Sears CM, Lei NY, Lewis M, et al. Type I collagen as an extracellular matrix for the in vitro growth of human small intestinal epithelium. *PLoS One* 2014;9(9):e107814.
- [38] Dudley AC. Tumor endothelial cells. *Cold Spring Harb Perspect Med* 2012;2(3):a006536.
- [39] Gaengel K, Niaudet C, Hagikura K, Laviña B, Muhl L, Hofmann JJ, et al. The sphingosine-1-phosphate receptor S1PR1 restricts sprouting angiogenesis by regulating the interplay between VE-cadherin and VEGFR2. *Dev Cell* 2012;23(3):587–99.
- [40] Massari F, Ciccarese C, Santoni M, Lopez-Beltran A, Scarpelli M, Montironi R, et al. Targeting fibroblast growth factor receptor (FGFR) pathway in renal cell carcinoma. *Expert Rev Anticancer Ther* 2015;15(12):1367–9 [Epub 2015/11/17].
- [41] Di Lisi D, Madonna R, Zito C, Bronte E, Badalamenti G, Parrella P, et al. Anticancer therapy-induced vascular toxicity: VEGF inhibition and beyond. *Int J Cardiol* 2017;227:11–7 [Epub 2016/11/21].
- [42] Huang D, Ding Y, Li Y, Luo WM, Zhang ZF, Snider J, et al. Sunitinib acts primarily on tumor endothelium rather than tumor cells to inhibit the growth of renal cell carcinoma. *Cancer Res* 2010;70(3):1053–62.
- [43] Keisner SV, Shah SR. Pazopanib. *Drugs* 2011;71(4):443–54.
- [44] Minkin P, Zhao M, Chen Z, Ouwerkerk J, Gelderblom H, Baker SD. Quantification of sunitinib in human plasma by high-performance liquid chromatography–tandem mass spectrometry. *J Chromatogr B* 2008;874(1):84–8.
- [45] Moreno Garcia V, Basu B, Molife LR, Kaye SB. Combining antiangiogenics to overcome resistance: rationale and clinical experience. *Clin Cancer Res* 2012;18(14):3750–61 [Epub 2012/05/02].
- [46] Clarke JM, Hurwitz HI. Understanding and targeting resistance to anti-angiogenic therapies. *J Gastroint Oncol* 2013;4(3):253–63 [Epub 2013/09/03].
- [47] Robinson SP, Boulton JKR, Vasudev NS, Reynolds AR. Monitoring the vascular response and resistance to Sunitinib in renal cell carcinoma in vivo with susceptibility contrast MRI. *Cancer Res* 2017;77(15):4127–34 [Epub 2017/06/02].
- [48] Doherty GJ, Lynskey D, Matakidou A, Fife K, Eisen T. Dose escalation of axitinib on disease progression as a strategy in the treatment of metastatic renal cell carcinoma. *ESMO Open* 2018;3(7):e000445.
- [49] Shojaei F. Anti-angiogenesis therapy in cancer: current challenges and future perspectives. *Cancer Lett* 2012;320(2):130–7.
- [50] Cruz SM, Tang YZ, Sarker S-J, Prevoo W, Kiyani I, Beltran L, et al. Heterogeneous response and progression patterns reveal phenotypic heterogeneity of tyrosine kinase inhibitor response in metastatic renal cell carcinoma. *BMC Med* 2016;14(1):185.
- [51] Menyhart O, Harami-Papp H, Sukumar S, Schäfer R, Magnani L, de Barrios O, et al. Guidelines for the selection of functional assays to evaluate the hallmarks of cancer. *Biochim Biophys Acta (BBA)* 2016;1866(2):300–19.
- [52] Dalton W. The influence of the tumor microenvironment on drug response and drug resistance. *AACR*; 2008.
- [53] Nyberg P, Salo T, Kalluri R. Tumor microenvironment and angiogenesis. *Front Biosci* 2008;13(7):6537–53.
- [54] Ayuso JM, Gillette A, Lugo-Cintrón K, Acevedo-Acevedo S, Gomez I, Morgan M, et al. Organotypic microfluidic breast cancer model reveals starvation-induced spatial-temporal metabolic adaptations. *EBioMedicine* 2018;37:144–57.
- [55] Motzer RJ, Escudier B, McDermott DF, George S, Hammers HJ, Srinivas S, et al. Nivolumab versus Everolimus in advanced renal-cell carcinoma. *N Engl J Med* 2015;373(19):1803–13 [Epub 2015/09/26].

- [56] Essig M, Terzi F, Burtin M, Friedlander G. Mechanical strains induced by tubular flow affect the phenotype of proximal tubular cells. *Am J Physiol Renal Physiol* 2001;281(4):F751–62 [Epub 2001/09/13].
- [57] Jang KJ, Cho HS, Kang DH, Bae WG, Kwon TH, Suh KY. Fluid-shear-stress-induced translocation of aquaporin-2 and reorganization of actin cytoskeleton in renal tubular epithelial cells. *Integr Biol (Camb)* 2011;3(2):134–41 [Epub 2010/11/17].
- [58] Kim S, LesherPerez SC, Kim BCC, Yamanishi C, Labuz JM, Leung B, et al. Pharmacokinetic profile that reduces nephrotoxicity of gentamicin in a perfused kidney-on-a-chip. *Biofabrication* 2016;8(1):015021.
- [59] Frohlich EM, Zhang X, Charest JL. The use of controlled surface topography and flow-induced shear stress to influence renal epithelial cell function. *Integr Biol* 2012;4(1):75–83.
- [60] Chistiakov DA, Orekhov AN, Bobryshev YV. Effects of shear stress on endothelial cells: go with the flow. *Acta Physiol (Oxf)* 2017;219(2):382–408 [Epub 2016/06/02].